Progress In Electromagnetics Research M, Vol. 136, 86–94, 2025

PIER M

(Received 6 October 2025, Accepted 11 November 2025, Scheduled 19 December 2025)

Dual-mode $BaTiO_3$ Ceramic Filter with Gold-copper Metallization

Víctor D. Vazquez Pereira[1,*], Marcelo E. Chávez[2], Sebastián Murcia[3], Jordi Verdú[1], and Pedro de Paco[1]

[1] *1Department of Telecommunications and Systems Engineering, Universitat Autònoma de Barcelona, 08193 Barcelona, Spain*
[2] *Catalonia Energy Research Institute (IREC), 08930 Sant Adrià de Besòs, Spain*
[3] *Catalan Institute of Nanoscience and Nanotechnology (ICN2), UAB Campus, 08193 Bellaterra, Spain*

ABSTRACT: In the design and fabrication of ceramic filters, the quality of metallization is crucial to minimize resistive losses and ensure optimal resonator performance. This work presents the design and fabrication of a monoblock dual-mode filter with two distinct types of couplings, based on barium titanate ($BaTiO_3$) ceramics, operating at S-band frequencies. Sputtering deposition was used to create a 5 nm gold seed layer, on which a 30 µm copper metallization was grown through electroplating. This method guarantees high conductivity in the resonator coating, and test results demonstrated that the fabricated device offers very good filtering performance with a minimal insertion loss of 0.57 dB.

1. INTRODUCTION

The growing demand for efficient frequency spectrum management, combined with the presence of numerous radio frequency circuits operating within the same system, drives the need for more compact and efficient devices. This requirement is even more critical in satellite applications and 5G/6G base stations, where system miniaturization and weight reduction are achieved by decreasing the size of individual components. Traditionally, partially dielectric-loaded cavity filters require a metallic housing and, in some cases, support materials with a low dielectric constant [1, 2]. Therefore, to further reduce the volume and mass of the filter, metallic coating represents a promising solution. Metallized ceramic dielectric filters have gained importance due to their excellent performance, miniaturization capability, low insertion loss, and high quality factor, as reported in [3–5], making them a topic of considerable interest in recent years.

However, the performance of the device is determined both by the properties of the dielectric materials used in its fabrication and by the quality of the metallization process. Silver paste is commonly used to metallize the surface of devices, but it typically does not achieve high conductivity and requires elevated temperatures during the sintering process, as explained in a previous work [6]. Due to the need for more efficient ceramic metallization methods, a previous study [7] explored a metal coating process for zirconium oxide (ZrO_2) ceramics and evaluated its conductive behavior under different surface roughness conditions. Nevertheless, the operational validation of this process in functional radio frequency devices is crucial to understanding its advantages and limitations.

In this context, this work proposes the fabrication of a filter based on high-permittivity ceramics, such as barium titanate ($BaTiO_3$), using a multilayer gold/copper/gold coating through the combination of two well-known techniques: sputtering and electroplating, in order to achieve a uniform and highly conductive metallization. Using electromagnetic simulation tools, a fully dielectric-loaded and ultra-compact resonator is designed, which exploits the first three resonant modes of the cavity, as shown in Figs. 1(a), 1(b), 1(c), and 1(d). This resonator is used to fabricate a second-order dual-mode filter with slot coupling, and a fourth-order filter with transmission zeros located above the passband.

2. RESONATOR METALLIZATION

$BaTiO_3$ is a ferroelectric ceramic material with photorefractive effects and piezoelectric properties [8]. Despite its high dielectric constant, pure $BaTiO_3$ acts as an insulator [9], complicating the deposition of conductive metals on its surface. To address this, the metallization process was performed in two distinct stages. First, a conductive layer was created on the ceramic surface to enable the subsequent deposition of the primary conductor. This initial conductive layer consisted of a 5 nm gold seed layer, applied via magnetron sputtering. Second, copper electrodeposition thickened the metallic coating to 35 µm. An additional gold layer was deposited through sputtering to prevent the copper layer from oxidation, as illustrated in Fig. 2. Before metallization, the $BaTiO_3$ piece underwent pretreatment to remove organic and inorganic impurities. This was achieved using an ultrasound bath with ultrapure water and acetone for 10 minutes [10]. Images and dimensions of the metallic layers were obtained by SEM (Field emission Zeiss Auriga series instrument). All electrochemical experiments were conducted at room temperature using a BioLogic electrochemical workstation.

---

[*] Corresponding author: Víctor Daniel Vazquez Pereira (Victor-Daniel.Vazquez@autonoma.cat).

doi:10.2528/PIERM25100601

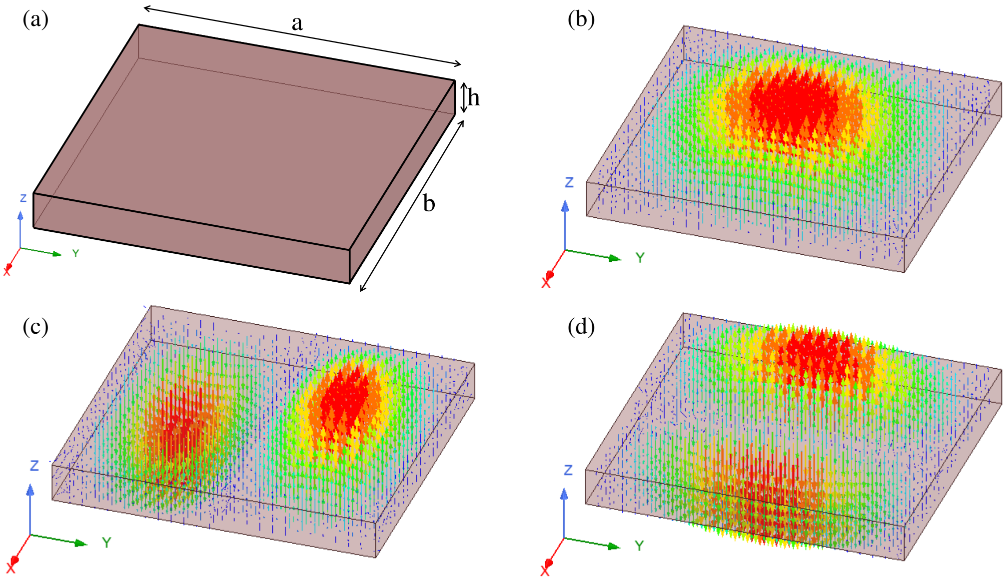

FIGURE 1. Dual mode resonator isometric view: (a) Cavity dimensions; (b) Electric field distribution TE_{110}; (c) TE_{120}; (d) TE_{210}.

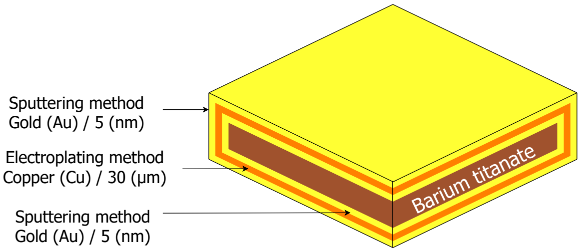

FIGURE 2. Metallization scheme with gold, copper, and gold layers.

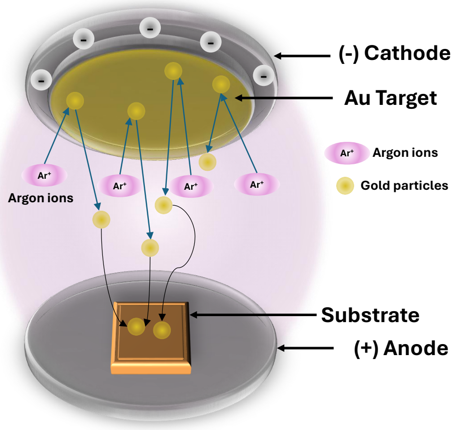

FIGURE 3. Gold sputtering process on a $BaTiO_3$ substrate.

2.1. Sputtering Deposition

Since ceramic materials are electrically insulating and chemically inert [11], this initial gold layer is essential as it provides an intermediate conductive surface. Without this preliminary step, the electroplating process would be unfeasible, as adequate adhesion and uniformity of the metallic coating could not be ensured. Sputtering, or cathodic sputtering, is a physical vapor deposition technique used to apply thin layers of material onto a surface or substrate. The process involves high-energy ion bombardment, where atoms from the surface of a solid material (target) are ejected and then deposited as a uniform layer onto another material, as shown in Fig. 3.

The gold seed layer is deposited by sputtering over the smooth surface of the $BaTiO_3$ piece using the equipment shown in Fig. 4(a) (Emitech Quorum Sputtering Machine). The configuration used consisted of a circular gold target, with a pressure inside the chamber of 2×10^{-2} millibar, a working current of 85 mA, and an exposure time of 4 minutes (2 minutes on each side), achieving a thickness of 5 nm. The result of this first layer can be observed in Fig. 4(b).

2.2. Electroplating Deposition

The deposition of the copper layer onto the gold seed layer was carried out using a procedure that involves placing the previously gold-coated piece in a cell prepared for this purpose, as shown in Fig. 5(a). The electroplating was performed in galvanostatic mode, using a copper plate as the anode electrode and the gold-coated piece as the cathode electrode, with a solution of 0.6 M $CuSO_4$ + 0.8 M H_2SO_4, and a working current of 70 mA, for 4 hours. During the deposition, the Cu^{2+} ions present in the solution were reduced to Cu^0 on the gold surface of the piece. The thickness of the metal coating is substantially increased, ranging from a few nanometers to 30 μm, which significantly enhances conductivity and adhesion to the ceramic. It is important to note that the final thickness of the layer and the high conductivity depend on several factors, such as the exposure time, the current used, and the composition of the solution, including the proportion of copper sulfate and sulfuric acid. Additionally, to prevent oxidation of the copper layer, a post-treatment is carried out, consisting of cleaning with pure water, initial drying with compressed N_2, and finally, inside a vacuum oven at 60°C for 2 hours, to obtain a result like that in

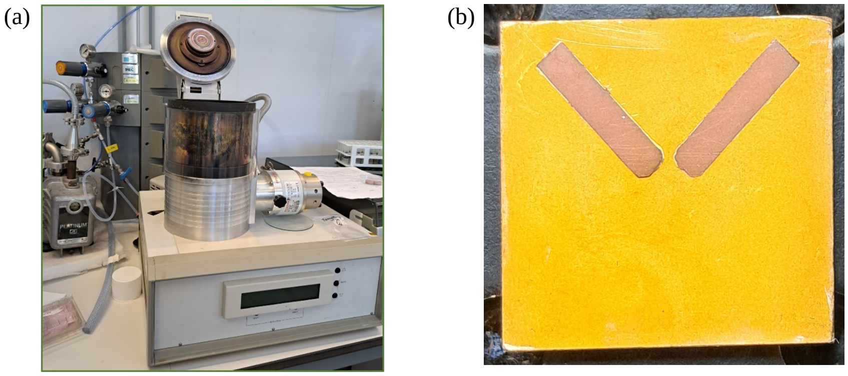

FIGURE 4. (a) Sputtering machine and (b) Gold plated $BaTiO_3$.

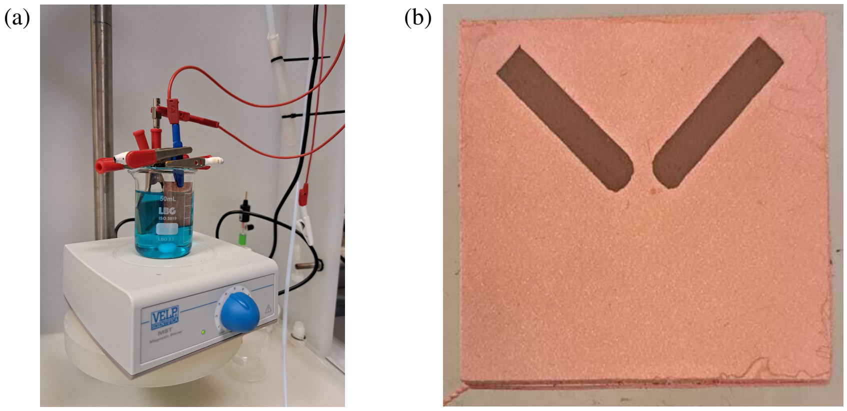

FIGURE 5. (a) Electroplating setup and (b) Copper plated $BaTiO_3$.

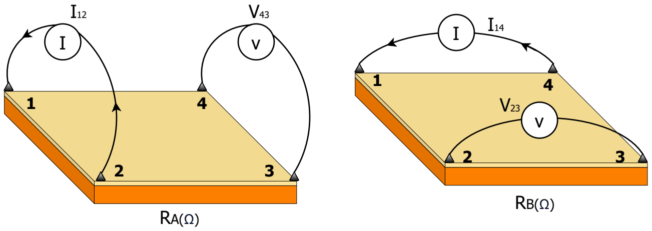

FIGURE 6. Conductivity measurement of a rectangular geometry sample using the Van der Pauw method.

Fig. 5(b). Finally, the sputtering process is repeated to apply a final layer of gold, which prevents oxidation of the copper.

2.3. Conductivity Measurement

The metallization was characterized using the Van der Pauw method [12, 13] for rectangular geometries. This procedure allows obtaining the resistivity of a sheet from the measured resistance values using the Van der Pauw Equation (1). For this purpose, fine-tipped probes are used at the four corners of the sample, and the resistance is measured, as shown in Fig. 6.

$$e^{-\pi\frac{R_A d}{\rho}} + e^{-\pi\frac{R_B d}{\rho}} = 1 \tag{1}$$

Four consecutive measurements are taken for each of the configurations, where a known current is supplied to two adjacent sides of the sample, and the voltage is measured on the side opposite to the current probe. The average resistances R_A and R_B are calculated from these values for the configurations, as indicated in (2) and (3).

$$R_A = \frac{1}{4}\left(\frac{V_{12}}{I_{43}} + \frac{V_{21}}{I_{34}} + \frac{V_{34}}{I_{21}} + \frac{V_{43}}{I_{12}}\right) \tag{2}$$

$$R_B = \frac{1}{4}\left(\frac{V_{23}}{I_{14}} + \frac{V_{32}}{I_{41}} + \frac{V_{14}}{I_{23}} + \frac{V_{41}}{I_{32}}\right) \tag{3}$$

An important factor in calculating resistivity using the Van der Pauw method is the thickness of the metal layer, which was measured using scanning electron microscopy and energy-dispersive X-ray spectroscopy (SEM/EDX) on ZEISS equipment, as shown in Fig. 7.

From this resistivity, conductivity can be obtained as its inverse, where R_A and R_B are the resistances measured in the test configurations, d is the thickness of the sheet, and ρ is the resistivity of the sheet that needs to be determined. In the measurement configuration, a direct current was supplied, performing a sweep from 10 mA to 200 mA.

This sweep is important because the minimum required current value to enter the ohmic region is initially unknown, where the relationship between the applied current and the measured voltage is flat. This ensures that the measured resistances accurately reflect the resistivity of the material, which is essential for obtaining consistent measurements and for the validity of the

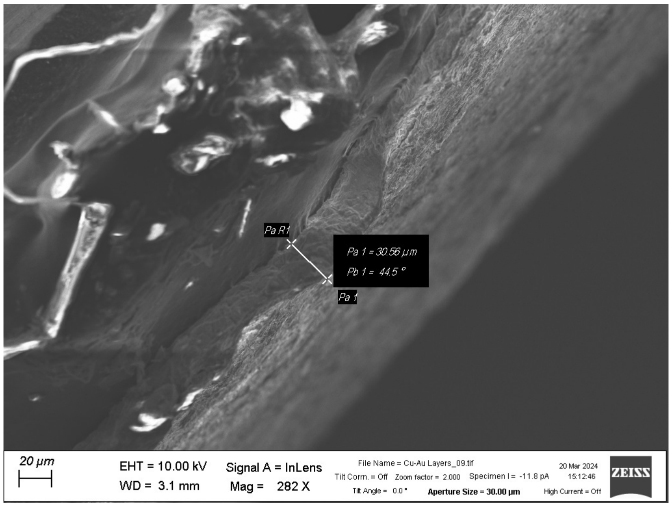

FIGURE 7. Image of the coating obtained using scanning electron microscopy.

Van der Pauw equation. According to Fig. 8 as one approaches this region, the conductivity tends to a value of 4.1×10^7 S/m for this experiment.

3. DUAL-MODE MONOBLOCK RESONATOR

For functional validation, the design of a dual TE mode filter is proposed, starting with a monolithic ceramic structure with a square prism geometry, fully metallized, and with initial dimensions of 25 mm × 25 mm × 3 mm. This structure, resembling a waveguide section, provides the fundamental mode TE_{110} and higher-order degenerate modes TE_{120} and TE_{210} [14]. These modes share the same resonance frequency but have orthogonal field distributions due to the symmetry of the structure [15], allowing the realization of dual resonators within the same physical resonator. In practice, this degeneracy can be broken by introducing perturbations or changes in operating conditions, a phenomenon known as mode splitting.

The frequency division of modes can be achieved in various ways, such as through the use of anisotropic materials, external coupling methods, changes in operating conditions, or imperfections and variations in geometry. In this work, we focus on introducing controlled geometric modifications to the structure to effectively adjust the resonance frequency of the degenerate modes, which is of particular interest for the design of dual-mode filters. These perturbations can be implemented in different ways, such as modifying one of the square dimensions, turning it into a rectangle, in order to separate the resonance frequencies while maintaining the orthogonality of the field distribution patterns.

Considering the need for a simple structure, a rectangular monolithic ceramic structure was chosen. This structure provides two poles and two transmission zeros by leveraging the three involved modes: TE_{110}, TE_{120}, and TE_{210}, as shown in Figs. 1(b), 1(c), and 1(d). The resonant frequencies of these modes, based on rectangular waveguide theory [16], can be calculated using (4). This allows for the implementation of asymmetric and fully canonical filtering functions.

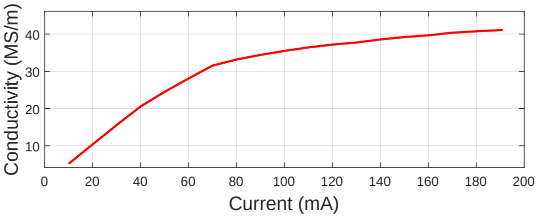

FIGURE 8. Conductivity values obtained using the Van der Pauw method.

$$fc = \frac{c}{2\pi\sqrt{\epsilon_r}}\sqrt{\left(\frac{m\pi}{a}\right)^2 + \left(\frac{n\pi}{b}\right)^2} \tag{4}$$

The modes are independent of the Z direction, meaning that the length in this dimension does not affect the resonant frequency. However, in Fig. 9, it is observed that the resonant frequencies of the TE_{120} and TE_{210} modes, simulated in under different lengths of dimension a (while keeping b constant), separate when the symmetry between the length and width of the structure is broken, maintaining orthogonality between them. This allows for control over the resonant frequencies of the degenerated modes, as well as the bandwidth. In Fig. 1(a), the dimensions are presented as follows: length $a = 23$ mm, width $b = 25$ mm, and height $c = 3$ mm. The dielectric material used has a relative permittivity of $\varepsilon_r = 37$ and a loss tangent of $\tan\delta = 1.5 \times 10^{-4}$. The unloaded quality factor Q for the TE_{120} and TE_{210} modes as a function of the resonator dimensions, obtained through EM simulation, is shown in Fig. 10. Considering the selected dimensions for this design, the resonant frequencies of the first three modes are $f_{TE110} = 1.455$ GHz, $f_{TE120} = 2.243$ GHz, and $f_{TE210} = 2.358$ GHz, and the unloaded quality factors obtained from simulations are $Q_{TE110} = 1108$, $Q_{TE120} = 1378$, and $Q_{TE210} = 1397$.

The combination of resonant and non-resonant modes in cavities has been explored in studies such as [17] and [18], which demonstrate how the arrangement of single-mode cavities enables the generation of both a transmission zero and a reflection zero. This approach takes advantage of the benefits of TE dual-mode cavities, which not only inherit the properties of dual modes but also incorporate additional functionalities arising from the use of non-resonant modes.

According to the electromagnetic field distribution of the structure, this TE dual-mode cavity is excited through two orthogonal feed slots. Depending on the positions of the input and output slots, both resonant and non-resonant modes can be appropriately excited to achieve fully canonical filtering functions with a pair of real-frequency transmission zeros.

4. SLOT-COUPLED DUAL-MODE FILTER

One way to efficiently excite the resonator is by using the slot coupling scheme [19]. As shown in Fig. 11, it consists of a dielectric substrate with a relative permittivity of $\varepsilon_r = 3.41$, a ground plane, and a feed line on the bottom side of the substrate. On the top face of the substrate, the line is electromagnetically coupled through a slot located in the ground plane, which is

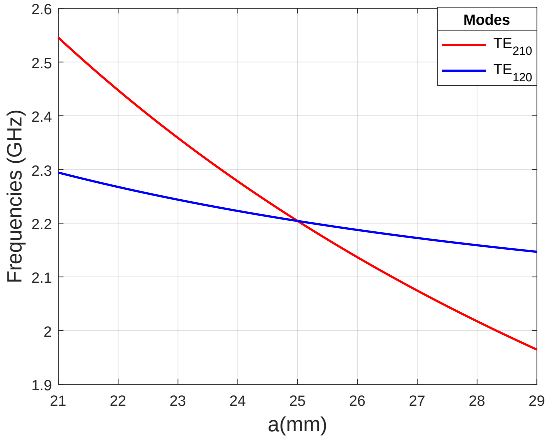

FIGURE 9. Frequency separation of the degenerate modes TE_{120} and TE_{210}.

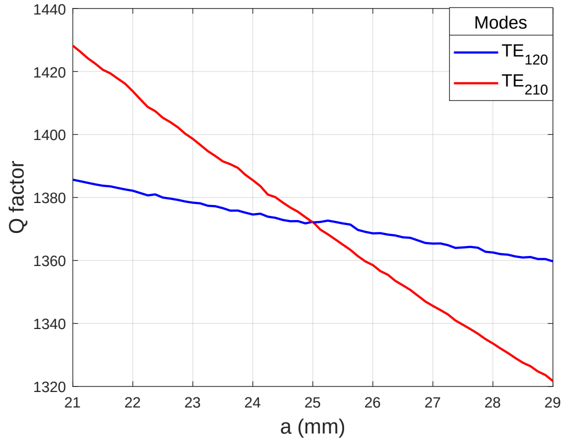

FIGURE 10. Quality factor of the TE_{120} and TE_{210} degenerate modes.

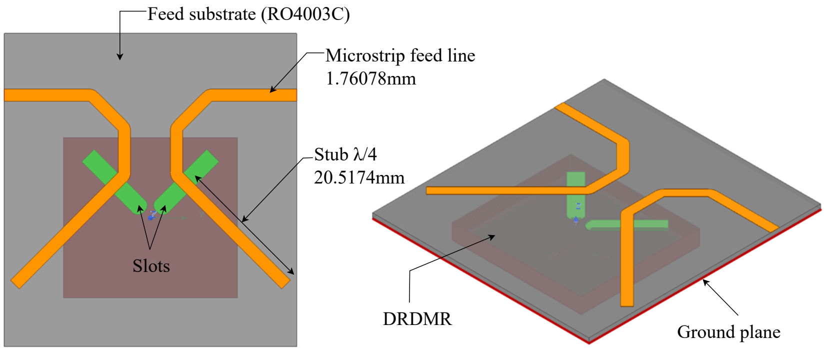

FIGURE 11. EM model with the opening coupling feeding scheme.

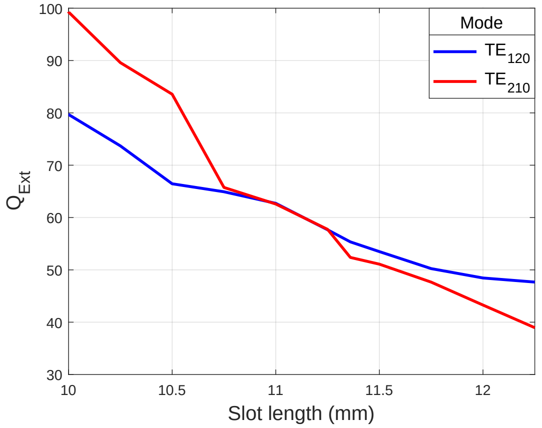

FIGURE 12. Simulated external quality factors for a slot width of 2.2 mm and varying slot lengths.

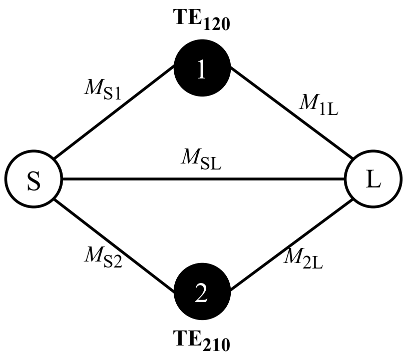

FIGURE 13. Starting topology.

positioned perpendicular and centered with respect to the feed line. It is important that the $\frac{\lambda}{4}$ stub, terminated in an open circuit, is centered within the slot to optimize the coupling.

It is essential to correlate a controllable physical parameter with the external coupling coefficients. This relationship allows defining the optimal input/output coupling level between the excitation system and the resonator, considering (5). The use of the group delay method described in [16] enables establishing the necessary link between these physical parameters through the values of the external quality factor Q_{Ext} and the normalized impedance using (6), which in this case can be calculated as a function of the slot lengths, as illustrated in Fig. 12.

$$Q_e = \frac{f_0}{BW \times M_{Si}^2} \tag{5}$$

$$\tau_{\max} = \tau(\omega_0) = \frac{4Q_e}{\omega_0} \tag{6}$$

The starting topology of the dual-mode filter is shown in Fig. 13. The coupling coefficients satisfy $M_{S1} = M_{L1}$ and

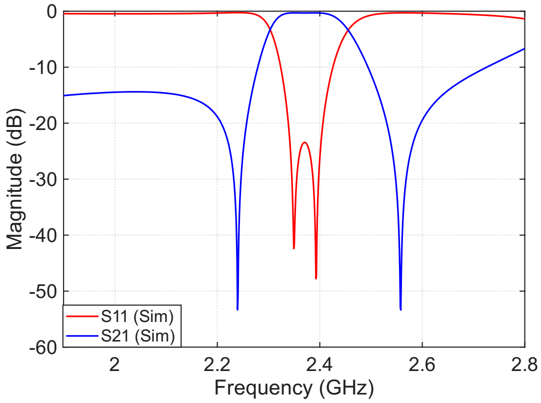

FIGURE 14. Comparison of the coupling matrix response with the electromagnetic simulation results.

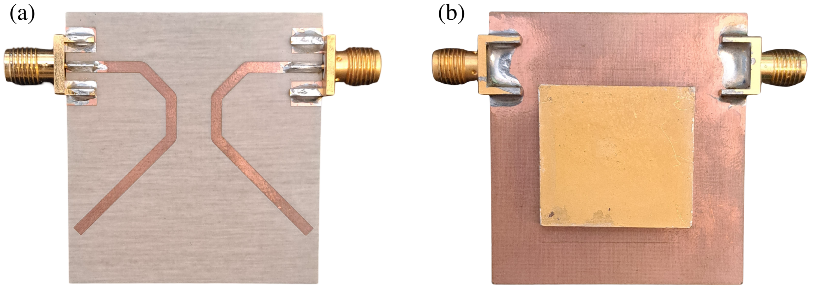

FIGURE 15. Fabricated prototype of the second-order filter: (a) Bottom view and (b) Top view.

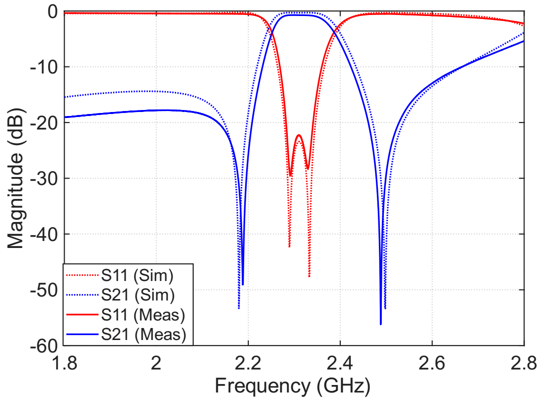

FIGURE 16. The simulation results were compared with the measurements carried out using a vector network analyzer.

$-M_{S2} = M_{L2}$, due to the fact that the electric field direction of the TE$_{120}$ mode is identical at the input (S) and output (L) ports, whereas for the TE$_{210}$ mode, the opposite is true. In addition, there is a direct source-load coupling M_{SL}, achieved through a reactive energy path generated by the TE$_{110}$ mode, which resonates out of band. This enables the introduction of an additional transmission zero, thus achieving a fully canonical transfer function with two transmission zeros, one on each side of the band.

Considering the electric field distribution, and following a scheme similar to that described in [20], when the excitation slot is placed on the XY plane with a 45° inclination, it is possible to simultaneously excite the first three resonant modes. In this design, the external coupling is achieved through an appropriate combination of slot lengths and their positioning on one face of the structure. The resonant frequencies of the TE$_{120}$ and TE$_{210}$ modes, which define the filter's operating band, can be approximated by physical parameters that can be directly obtained from Fig. 9. The transfer function response corresponding to the topology shown in Fig. 14 exhibits the following characteristics: $f_0 = 2.306\,\text{GHz}$, $BW = 61.2\,\text{MHz}$, $FBW = 2.65\%$, and $RL = 23.4\,\text{dB}$.

Figure 16 shows the comparison between the coupling matrix response and the electromagnetic simulation results, demonstrating a strong agreement between both approaches.

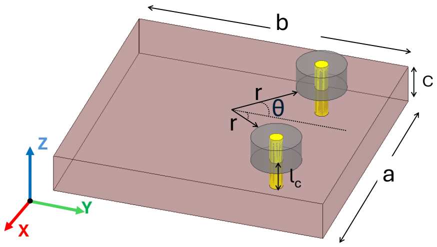

FIGURE 17. Isometric view of the EM model with coaxial probe coupling.

4.1. Experimental Results

Finally, in Figs. 15(a) and 15(b), the fabricated prototypes with the corresponding assembly are shown. Additionally, in Fig. 16, the comparison between the measured filtering response of the fabricated prototype and the EM simulation is presented, showing a good agreement between both. The filter has a $FBW = 2.33\%$, the measured RL in the band is 22.3 dB, and the $IL = 0.63\,\text{dB}$, with $f_0 = 2.310\,\text{GHz}$ and a $BW = 54.0\,\text{MHz}$. The measured quality factor is 1058. The final size of the filter, excluding the feed structure, is $24.28 \times 22.8 \times 3\,\text{mm}$. The small variations observed in the response can be attributed to the inherent tolerances in the manufacturing process, assembly, and the physical properties of the materials used.

5. COAXIAL-PROBE COUPLED DUAL-MODE FILTER

Another common technique to achieve external coupling in this type of filters is the use of a coaxial probe inserted into the cavity. By properly positioning the probe in a region of the electric field and adjusting its length and orientation, it is possible to simultaneously excite the desired resonant modes, such as the TE$_{110}$, TE$_{120}$, and TE$_{210}$ modes.

This mechanism can be observed in Fig. 17, where $a = 20\,\text{mm}$, $b = 21\,\text{mm}$, and the height is $c = 3\,\text{mm}$. Moreover, the ports are placed symmetrically with respect to the horizontal axis, with an angle $\theta = 45°$ and at a distance $r = 7.5\,\text{mm}$ from the center of the structure. This configuration allows the implementation of the same topology shown in Fig. 17, but with the

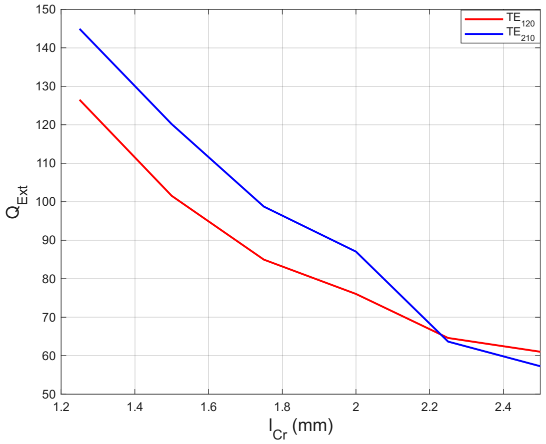

FIGURE 18. Simulated external quality factors for different values of coaxial-probe coupling.

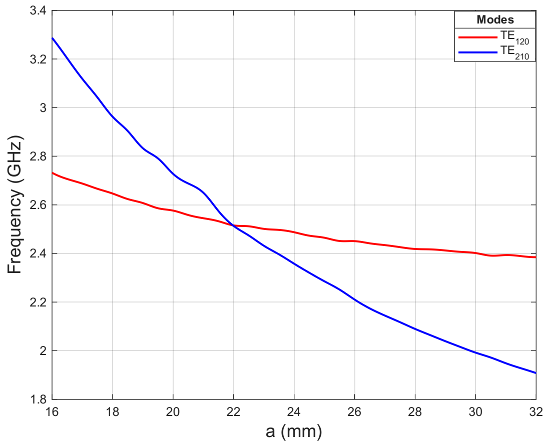

FIGURE 19. Frequency separation of the degenerate modes TE_{120} and TE_{210}.

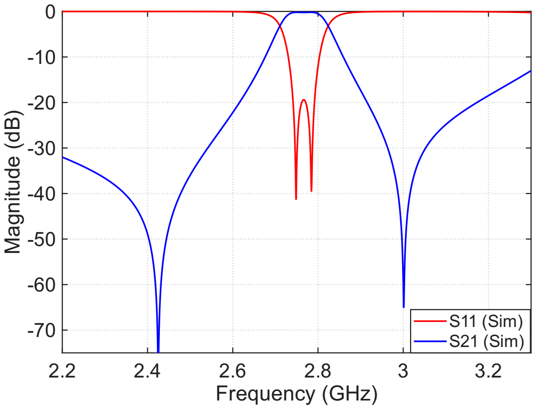

FIGURE 20. Electromagnetic simulation response of a dual-mode TE cavity.

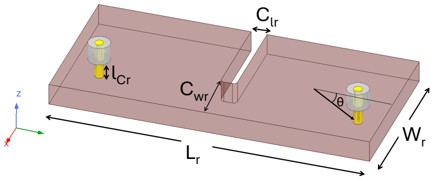

FIGURE 21. Isometric view of the fourth-order monolithic filter with two resonators.

coupling coefficients and eigenvalues determined by this particular structure. In this case, the external coupling values are defined by the length l_{Cr}, as shown in Fig. 18. The resonant frequencies that form the passband are controlled in a similar manner by varying one of the cavity dimensions while keeping the other constant, in order to achieve frequency separation of the degenerate modes, as illustrated in Fig. 19.

The transfer function response described in the topology shown in Fig. 13 exhibits a filtering behavior with $f_0 = 2{,}69\,\text{GHz}$, $BW = 44{,}1\,\text{MHz}$, $FBW = 1{,}63\%$, and $RL = 21{,}69\,\text{dB}$. In Fig. 20, a comparison between the coupling matrix response and the electromagnetic simulation results can be observed, showing excellent agreement.

6. FOURTH-ORDER DUAL-MODE FILTER

This section presents the design of an asymmetric fourth-order filter with transmission zeros (TZs) located above the passband. The same basic rectangular resonator structure is employed, which allows the construction of higher-order filters by cascading blocks through a coupling iris [21]. Fig. 21 shows the top and isometric views of the filter designed with the EM simulator. La estructura consiste en dos cavidades de modo dual, alineadas horizontalmente y acopladas mediante un iris. Differentiating it from other designs, this simple structure does not require additional blind holes for adjustment, only those necessary to place the connectors, making fabrication easier. The physical dimensions of the structure are: $L_r = 44.2\,\text{mm}$, $W_r = 20.5\,\text{mm}$, $C_{wr} = 7.8\,\text{mm}$, $C_{lr} = 2.2\,\text{mm}$, $r = 6.7\,\text{mm}$, and $l_{cr} = 2.7\,\text{mm}$, with the coaxial connectors rotated at an angle $\theta = 110^\circ$ around the cavity center. The filter was designed with the following characteristics: $f_0 = 2.61\,\text{GHz}$, $BW = 127.1\,\text{MHz}$, $FBW = 4.9\%$, $IL = 0.18\,\text{dB}$.

6.1. Transmission Zero Tuning

In the proposed filter, the tuning of the transmission zeros is achieved by modifying the angle θ, which defines the relative position of the input and output ports. These ports are symmetrically displaced with respect to the horizontal axis of the resonator. Although this tuning cannot be performed completely independently — since the geometric parameters that determine the TZ positions also influence the reflection response — it still enables a meaningful degree of control over their frequency location.

By varying θ, one of the transmission zeros shifts while the other remains nearly constant, producing only a slight change in the reflection response and leaving the transmission response practically unaffected, as shown in Fig. 22. This mechanism enables tuning the location of the TZs and, consequently, improving the out-of-band attenuation without significantly degrading the in-band performance.

TABLE 1. Measured results in comparison with previous works.

References	Operative Modes	f_0 (GHz)	Filter Order	IL (dB)	RL (dB)	FBW (%)	Type	Dimensions (mm)
[3]	TE_{102}, TE_{201}	3.44	4	0.3	13	6	DRDMR	$46.4 \times 22.2 \times 8.5$
[5]	TM_{101}, TM_{102}, TM_{201}	4.98	3	0.63	20	13	DWR	$29 \times 8.5 \times 3$
[4]	TM_{120}, TM_{210}	3.55	4	-	25	2.54	DRDMR	$41.6 \times 20.8 \times 9.6$
This Work	TE_{110}, TE_{120}, TE_{210}	2.65	4	0.57	17	4.57	DWR	$44.1 \times 20.45 \times 3$

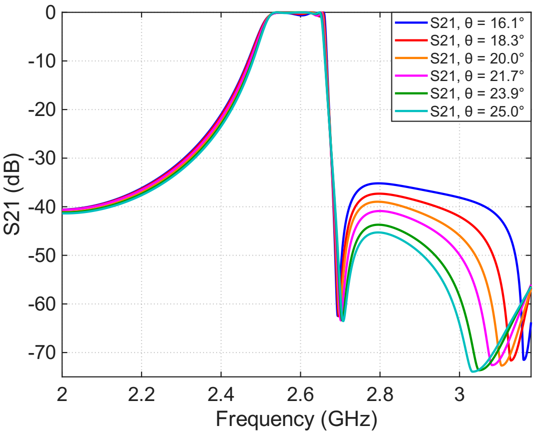

FIGURE 22. Simulated transmission coefficient S_{21} of the fourth-order filter for different port angles θ.

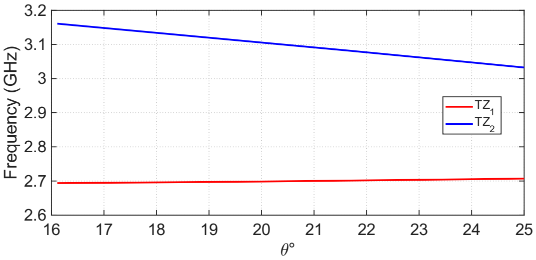

FIGURE 23. Evolution of the transmission zeros as a function of the port angle θ.

Figure 23 summarizes the behavior of both zeros as a function of θ. The first TZ, located near the passband, remains almost constant, ensuring high selectivity close to the band. In contrast, the second zero gradually moves away from the passband, enabling an increase in out-of-band attenuation without compromising the selectivity in the passband region.

6.2. Experimental Validation

To validate the proposed design concept, the filter was fabricated using the same barium titanate ceramic with identical dielectric properties. Since this material is extremely hard, abrasive water jet cutting was employed for the geometric profiling of the piece, a technique that proved to be highly efficient for machining hard ceramics without causing thermal or mechanical damage. The water jet, combined with abrasive particles, erodes the material with high precision and without generating heat, thus preserving the structural integrity of the ceramic.

FIGURE 24. Isometric view of the fabricated fourth-order filter with four transmission zeros located above the passband.

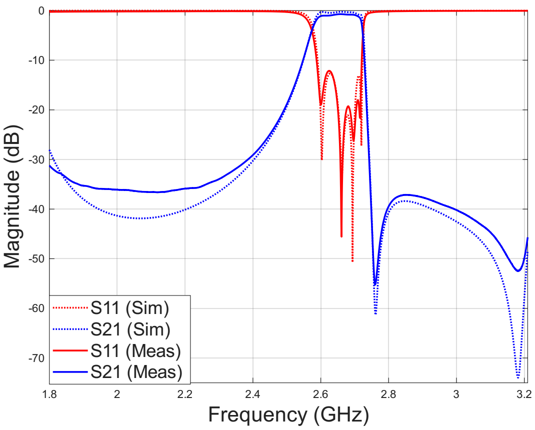

FIGURE 25. The simulation results were compared with the measurements carried out using a vector network analyzer.

On the other hand, the blind hole was drilled using a drill bit with a tolerance of ± 0.01 mm, after which the metallization process was performed following the methodology described in Section 2. The fabricated fourth-order filter is shown in Fig. 24. The input/output couplings are fixed and implemented through coaxial connectors matched to $50\,\Omega$.

The results obtained from the measurements, compared with the EM simulations, are shown in Fig. 25, where a good agreement between both is observed. The filter presents a $FBW = 4.57\%$, an insertion loss $IL = 0.57$ dB, a center frequency $f_0 = 2.65$ GHz, a bandwidth $BW = 121$ MHz and having two transmission zeros at 2.76 GHz and 3.17 GHz, respectively.The final size of the filter is $44.1 \times 20.45 \times 3$ mm. The small variations in the response can be attributed to imperfections and manufacturing tolerances. Table 1 presents the comparison with other dielectric filters, demonstrating that the proposed filter achieves very good performance in terms of bandwidth and out-of-band rejection while maintaining a reduced circuit size and a simple structure that does not require external tuning elements or blind holes.

7. CONCLUSION

A dual-mode resonator based on a rectangular waveguide section fully filled with dielectric material has been proposed. The metallization procedure employed ensures high conductivity of the plating. Furthermore, this resonator was used in the fabrication of second- and fourth-order filters using two different coupling mechanisms: slot coupling and coaxial probe coupling, which constitutes an advantage as it could enable greater integration possibilities in RF systems or subsystems, functionally validating the application of these techniques in filtering devices. All these contributions allow for simpler and more compact designs that enhance the capabilities of ceramic filters. The experimental results are consistent with the theoretical ones, confirming the feasibility of the proposed filter designs.

ACKNOWLEDGEMENT

Special thanks to Dr. Josep Parron Granados, Professor at the Department of Telecommunications and Systems Engineering of the Universitat Autònoma de Barcelona, for his valuable contributions.

This work has been supported by the Agencia Estatal de Investigación (AEI)-Ministerio de Ciencia e Innovación under Project PID2021-127203OB-I00 and PID2024-159605OB-I00.

REFERENCES

[1] Pelliccia, L., F. Cacciamani, C. Tomassoni, and R. Sorrentino, "Ultra-compact filters using TM dual-mode dielectric-loaded cavities with asymmetric transmission zeros," in *2012 IEEE/MTT-S International Microwave Symposium Digest*, 1–3, Montreal, QC, Canada, 2012.
[2] Pelliccia, L., F. Cacciamani, F. Vitulli, W. Steffè, F. Diaferia, E. Picchione, P. M. Iglesias, and A. Jones, "On-board miniaturized L-band input filter based on TM-mode dielectric resonator for MSS applications," in *2017 47th European Microwave Conference (EuMC)*, 981–984, Nuremberg, Germany, 2017.
[3] Xie, Y., F.-C. Chen, and Q.-X. Chu, "Inline box-like dielectric filters with asymmetric and symmetric responses," *IEEE Transactions on Microwave Theory and Techniques*, Vol. 71, No. 6, 2522–2531, 2023.
[4] Xie, Y. and F.-C. Chen, "Silver-plated dielectric waveguide filters using dual-ridge dual-mode resonator," in *2021 IEEE MTT-S International Microwave Filter Workshop (IMFW)*, 169–171, Perugia, Italy, 2021.
[5] Wang, C., H. Huang, and P. Wen, "Miniaturized broadband dielectric waveguide resonator bandpass filter with wide stopband using CPW resonator," *Progress In Electromagnetics Research C*, Vol. 157, 201–206, 2025.
[6] Zheng, Z., Y. Zhang, F. Yi, C. Chen, and X. Song, "Surface metallization of alumina ceramics: Effects of sintering time and substrate etching," *Ceramics International*, Vol. 40, No. 8, 12 709–12 715, 2014.
[7] Hou, H., H. Wang, B. Lin, T. Sui, X. Cui, H. Li, J. Ding, J. Wang, and J. Yang, "High quality surface metallization methods and performance evaluation for ceramic micro RF devices," in *2023 IEEE 16th Malaysia International Conference on Communication (MICC)*, 56–58, Kuala Lumpur, Malaysia, Dec. 2023.
[8] Chavez, M. E., M. Biset-Peiró, S. Murcia-López, and J. R. Morante, "Cu_2O-Cu@ titanium surface with synergistic performance for nitrate-to-ammonia electrochemical reduction," *ACS Sustainable Chemistry & Engineering*, Vol. 11, No. 9, 3633–3643, 2023.
[9] Karacasulu, L., M. Tokkan, M. Bortolotti, G. Ischia, U. Adem, and C. Vakifahmetoglu, "Electrical characteristics of low temperature densified barium titanate," *Ceramics International*, Vol. 46, No. 10, 16 670–16 676, 2020.
[10] Kim, J. J. and S.-K. Kim, "Optimized surface pretreatments for copper electroplating," *Applied Surface Science*, Vol. 183, No. 3–4, 311–318, 2001.
[11] Ali, H., M. Uzair, Y. Iqbal, M. Ali, and W. Ahmad, "Electrical properties of Barium titanate and graphite incorporated PVA matrix composite (PVA-$BaTiO_3$-G) nanofibers," *Materials Science and Engineering: B*, Vol. 296, 116655, 2023.
[12] Van der Pauw, L. J., "A method of measuring the resistivity and hall coefficient on lamellae of arbitrary shape," *Philips Technical Review*, Vol. 20, 220–224, 1958.
[13] Oliveira, F. S., R. B. Cipriano, F. T. D. Silva, E. C. Romão, and C. A. M. D. Santos, "Simple analytical method for determining electrical resistivity and sheet resistance using the van der pauw procedure," *Scientific Reports*, Vol. 10, No. 1, 16379, 2020.
[14] Slimane, G., D. Mehdi, C. Mohammed, and B. Abdelhakim, "Design of a bandpass rectangular waveguide filter based on direct coupled technique," *International Journal of Electronics and Telecommunications*, Vol. 68, No. 3, 483–488, 2022.
[15] Uher, J., J. Bornemann, and U. Rosenberg, *Waveguide Components for Antenna Feed Systems: Theory and CAD*, Artech House, 1993.
[16] Cameron, R. J., C. M. Kudsia, and R. R. Mansour, *Microwave Filters for Communication Systems: Fundamentals, Design, and Applications*, John Wiley & Sons, 2018.
[17] Amari, S. and U. Rosenberg, "Characteristics of cross (bypass) coupling through higher/lower order modes and their applications in elliptic filter design," *IEEE Transactions on Microwave Theory and Techniques*, Vol. 53, No. 10, 3135–3141, 2005.
[18] Rosenberg, U., S. Amari, and J. Bornemann, "Inline TM/sub 110/-mode filters with high-design flexibility by utilizing bypass couplings of nonresonating TE/sub 10/01/modes," *IEEE Transactions on Microwave Theory and Techniques*, Vol. 51, No. 6, 1735–1742, 2003.
[19] Pozar, D. M., "Microstrip antennas," *Proceedings of the IEEE*, Vol. 80, No. 1, 79–91, 1992.
[20] Bastioli, S., C. Tomassoni, and R. Sorrentino, "TM dual-mode pseudoelliptic filters using nonresonating modes," in *2010 IEEE MTT-S International Microwave Symposium*, 880–883, Anaheim, CA, USA, 2010.
[21] Guglielmi, M., P. Jarry, E. Kerherve, O. Roquebrun, and D. Schmitt, "A new family of all-inductive dual-mode filters," *IEEE Transactions on Microwave Theory and Techniques*, Vol. 49, No. 10, 1764–1769, 2001.